JGR Oceans

RESEARCH ARTICLE
10.1029/2025JC023684

Energetics of Internal Solitary Waves Interacting With a Conical Island

S. Tan[1,2], J. S. Rogers[3], O. B. Fringer[2,3], G. Pawlak[4,5], Y. Chang[4], and K. A. Davis[2,3]

[1]Department of Marine Sciences, University of Connecticut, Groton, CT, USA, [2]Department of Oceans, Stanford University, Stanford, CA, USA, [3]The Bob and Norma Street Environmental Fluid Mechanics Laboratory, Stanford University, Stanford, CA, USA, [4]Department of Mechanical and Aerospace Engineering, University of California San Diego, La Jolla, CA, USA, [5]Scripps Institution of Oceanography, University of California San Diego, La Jolla, CA, USA

Abstract The interaction of internal solitary waves (ISWs) with sloping topography plays a critical role in ocean mixing and energy dissipation. We use idealized simulations of an ISW shoaling on a conical island to analyze spatial energy pathways, with parameters based on observations at Dongsha Atoll in the South China Sea, which is located in the path of some of the world's largest ISWs. Results show that energy dissipation is highly heterogeneous, concentrated in shallow regions where the wave is normally incident and along the island flanks. Unlike two-dimensional slopes, three-dimensional topography enables partial conversion of baroclinic to barotropic kinetic energy on the wave-facing slope, driven by a longshore barotropic pressure gradient induced by shoaling. This conversion accounts for 20% of the total baroclinic energy divergence over the island. The resulting barotropic currents form recirculation cells that advect around the island and eventually transfer energy back into baroclinic kinetic energy along deeper flanks and the lee slope before dissipating. Earth's rotation further modulates the distribution of wave energy and barotropic flow patterns. Understanding these spatially variable energetics and wave-driven barotropic currents is essential for predicting energy pathways and transport mechanisms that influence cross- and along-shore exchange of nutrients and heat, with implications for sensitive island ecosystems.

Plain Language Summary Internal waves are oscillatory movements at interfaces between fluid layers of different densities. Internal solitary waves are typically hump-shaped and can maintain their form while traveling tens to hundreds of kilometers before breaking. These waves steepen and break in shallow coastal areas, playing a crucial role in ocean mixing and mass transport. Although their dynamics have been widely studied over two-dimensional topography, their interactions with three-dimensional features remain less understood. In this study, we use a numerical model to examine how and where the energy of these waves is transferred and lost to heat around a conical island representative of Dongsha Atoll in the South China Sea. For an east–west propagating wave that breaks on the island's eastern side, most of its energy is lost over slopes shallower than 180 m, with about half on the eastern slope and a quarter along the southern and northern sides. As the wave moves up the eastern slope, it drives a uniform, top to bottom current around the island. As this current travels along the island's flanks, it releases its energy to generate vertically varying flows. Earth's rotation further modifies the spatial distribution of wave energy transformation.

Key Points:

- The shoaling and breaking of internal solitary waves over three-dimensional topography causes spatially heterogeneous dissipation
- Shoaling over three-dimensional topography creates a longshore pressure gradient that drives barotropic currents
- Baroclinic-to-barotropic conversion occurs on the wave-facing side; the reverse happens along the island flanks

Supporting Information:

Supporting Information may be found in the online version of this article.

Correspondence to:

S. Tan,
shuwen.tan@uconn.edu

Citation:

Tan, S., Rogers, J. S., Fringer, O. B., Pawlak, G., Chang, Y., & Davis, K. A. (2026). Energetics of internal solitary waves interacting with a conical island. *Journal of Geophysical Research: Oceans*, *131*, e2025JC023684. https://doi.org/10.1029/2025JC023684

Received 31 OCT 2025
Accepted 4 APR 2026

Author Contributions:

Conceptualization: S. Tan, J. S. Rogers, O. B. Fringer, G. Pawlak, K. A. Davis
Formal analysis: S. Tan
Funding acquisition: O. B. Fringer, G. Pawlak, K. A. Davis
Investigation: S. Tan
Methodology: S. Tan, J. S. Rogers, Y. Chang
Project administration: J. S. Rogers, O. B. Fringer, G. Pawlak, K. A. Davis
Software: S. Tan, J. S. Rogers, Y. Chang
Supervision: K. A. Davis
Visualization: S. Tan
Writing – original draft: S. Tan
Writing – review & editing: J. S. Rogers, O. B. Fringer, G. Pawlak, Y. Chang, K. A. Davis

1. Introduction

Internal solitary waves (ISWs) are ubiquitous in the world's oceans (Alford et al., 2015; Magalhaes & Da Silva, 2018; McSweeney et al., 2020; Shroyer et al., 2011). They are most commonly generated through tide-topography interactions (Jackson et al., 2012). Once formed, ISWs can maintain a coherent waveform over long distances due to a balance between nonlinear steepening and nonhydrostatic dispersion, enabling the transport of energy well away from their source regions (Lamb et al., 2019). As they shoal and break over inner continental shelves, they dissipate energy through intense turbulent mixing that influences local ecosystems and resuspends sediments (Boegman & Stastna, 2019; Garwood et al., 2020; Lamb, 2014; Reid et al., 2019; Rogers et al., 2025). Internal wave shoaling and breaking are controlled by a combination of bathymetric slope, vertical density structure, background velocity shear, and the amplitude of the incoming wave (Aghsaee et al., 2010; He et al., 2019; S. K. Venayagamoorthy & Fringer, 2007). When ISWs shoal over gentle continental slopes (topographic slopes of 0.01–0.03; Boegman and Stastna (2019)), they may undergo a range of instabilities that develop either within the wave core or along the seabed (Lamb et al., 2019; Stastna & Legare, 2024). Such

instabilities include shear and convective instabilities associated with the wave core (e.g., Chang et al. (2021); Bolioudakis et al. (2026)), global instabilities that arise in the bottom boundary layer beneath the wave (Carr & Davies, 2010; Diamessis & Redekopp, 2006; Xu & Stastna, 2020), and transverse three-dimensional instabilities such as lobe-and-cleft and shear instabilities during breaking (Arthur & Fringer, 2014; Castro-Folker & Stastna, 2024; Lucas & Pinkel, 2022).

The energetics of shoaling and breaking ISWs on two-dimensional sloping topography has been extensively studied (Lamb & Nguyen, 2009; la Forgia et al., 2018; Michallet & Ivey, 1999; S. Venayagamoorthy & Fringer, 2005; S. K. Venayagamoorthy & Fringer, 2006). Generally, as an ISW shoals, it slows down, and kinetic energy is converted into available potential energy. The wave breaks as the available potential energy reaches its peak value, leading to energy dissipation and an increase in background potential energy due to turbulent mixing (Becherer et al., 2021a, 2021b; Kang & Fringer, 2010; Lamb & Nguyen, 2009). Over two-dimensional topography, the cross-slope energy flux divergence can be empirically considered equal to the energy dissipation, a relation recently used to parameterize energy losses upon internal tide shoaling at the continental shelf (Becherer et al., 2021b). The energetics of ISW shoaling over three-dimensional topography can be subject to energy flux occurring in the along-crest direction. Additionally, wave refraction and diffraction can redirect the incident wave energy (Vlasenko & Stashchuk, 2007; Wang & Legg, 2023), and the Earth's rotation can further alter wave characteristics and energy fluxes (Farmer et al., 2009; Helfrich, 2007). Rogers et al. (2022) also demonstrated that internal wave-induced residual flow can be strongly affected by rotation. When ISWs interact with three-dimensional sloping topography, the spatial distribution of energy dissipation will depend on both cross-slope and along-slope energy flux divergence (Kang & Fringer, 2012).

Here we investigate three-dimensional internal wave energetics through idealized numerical simulations of an ISW impinging upon a conical island, motivated by recent observations of ISW shoaling and breaking at Dongsha Atoll in the South China Sea (e.g., Davis et al. (2020); Sinnett et al. (2022)). Dongsha Atoll lies along the path of some of the largest ISWs in the world, which propagate toward the eastern side of the atoll. In the deep basin of the South China Sea, ISW amplitudes can exceed 150 m (Lien et al., 2014; S. R. Ramp et al., 2004; S. Ramp et al., 2010; S. Ramp et al., 2022), with typical values around 50 m (Li & Farmer, 2011). The depth-integrated available potential energy of ISWs was reported to be 18.8 MJ m^{-1} based on mooring data deployed at a site located at 285 m depth on the slope just east of the Dongsha Atoll (Fu et al., 2012). Cheng et al. (2024) further showed that a Dubreil-Jacotin-Long solution with a depth-integrated available potential energy of 130 MJ m^{-1} best matches satellite-derived ISW phase speed east of Dongsha Atoll. Notably, this estimated energy lies near the lower bound of the range reported by Lien et al. (2014) (121∼365 MJ m^{-1}) for ISWs observed over the continental slope north of Dongsha Atoll, where the waves are typically strongest. Several numerical simulations and in situ observations have been conducted on the eastern slope of the Dongsha Atoll to understand the characteristics and the fate of ISWs. For example, Davis et al. (2020) investigated the transformation of ISWs on the eastern slope of Dongsha Atoll using distributed temperature sensing (DTS), and showed that the observed wave characteristics compared well with results from a two-dimensional simulation forced by an incident wave with a depth-integrated available potential energy of 18.8 MJ m^{-1}. Sinnett et al. (2022) characterized the shoaling, breaking, and run-up of incident ISWs using data from moorings and DTS. However, these two-dimensional observations and simulations do not provide information on the wave characteristics or energetics at the northern and southern flanks and the western slope of the island. An important question that remains unanswered is how the breaking ISW-induced dissipation is distributed around the island. Rogers et al. (2022) utilized three-dimensional simulations to study the role of internal tides in driving residual flows, but did not analyze the full energy budget.

The structure of the paper is as follows. Section 2 details the model configuration and the energy budget equations. After presenting the two-dimensional energy budget along a transect on the eastern slope of the conical island in Section 3.1, Sections 3.2 and 3.3 describe the energy budget and baroclinic-to-barotropic energy conversion of the ISW steepening and shoaling at the island slopes. Section 3.4 compares the results with a two-dimensional slope run and highlights the role of three-dimensional topography in driving barotropic flows. Section 3.5 investigates the rotational effect on the shoaling ISW. Finally, a summary is provided in Section 4.

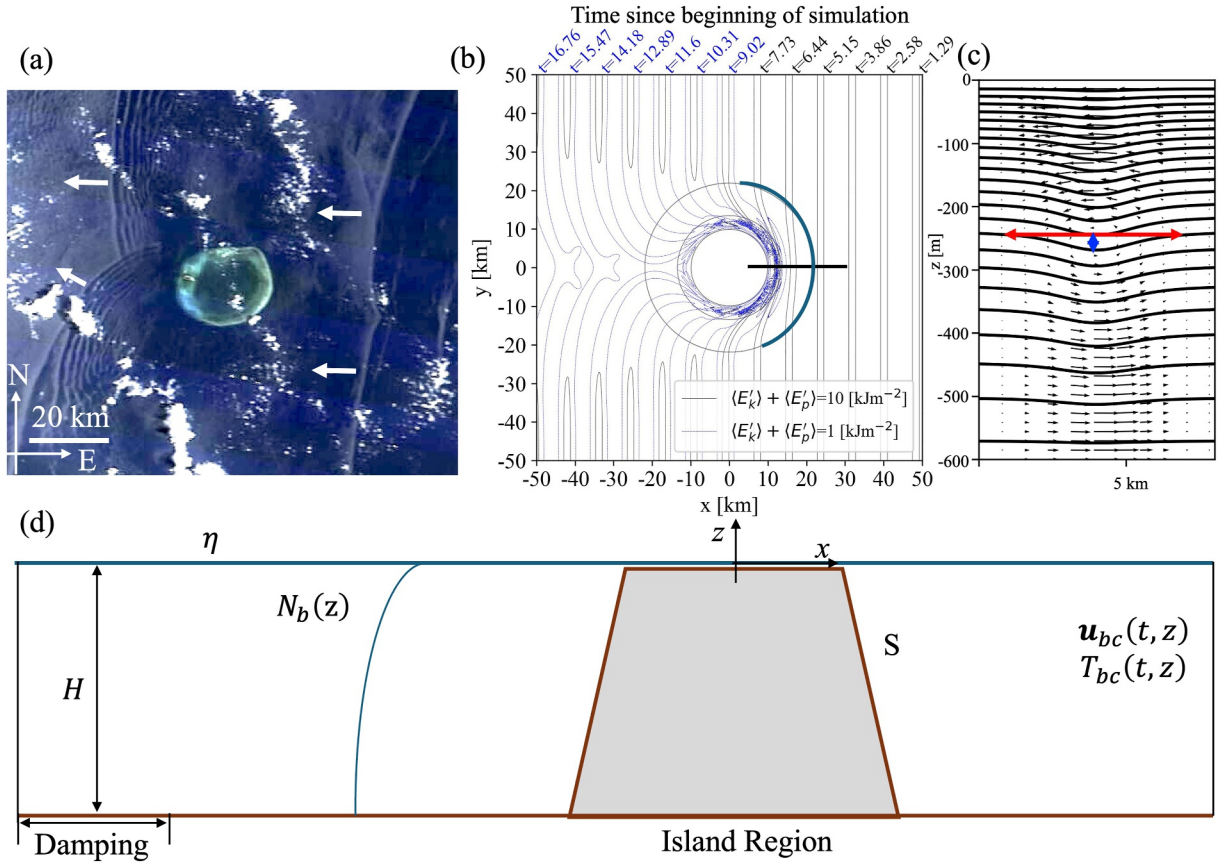

Figure 1. Representative satellite image of Dongsha Atoll showing internal solitary waves traveling from east to west (a), along with the model configuration for the idealized island domain (b), (d). The background stratification profile N_b is based on summer conditions in the northern South China Sea and is used to solve the DJL equation. The resulting DJL solutions are shown in (c), with temperature displayed as contours and velocity as arrows. Twice the wavelength L_w and the wave height A_w, used to estimate the Iribarren number, are indicted by red and blue double arrows, respectively. The model is forced at the boundary by horizontal velocity $\mathbf{u}_{bc}$ and temperature T_{bc}, based on the DJL solutions (c) and the corresponding wave speed. Panel (a) is taken from Terra/MODIS imagery from 26 May 2021 (https://worldview.earthdata.nasa.gov). The time evolution of wave crests, represented by the baroclinic energy contours, is shown in (b).

2. Methods

2.1. Numerical Model

This study employs the nonhydrostatic SUNTANS model (Fringer et al., 2006), which features a semi-implicit free-surface formulation that removes the stability restrictions of surface gravity waves and enables realistic simulations over fully three-dimensional bathymetry. These capabilities allow us to model an ISW interacting with a conical island in a setting that extends beyond the rigid-lid, two-dimensional configurations used in most prior ISW shoaling studies. The SUNTANS model has been previously employed to examine residual currents driven by shoaling internal tides around a conical island (Rogers et al., 2019, 2022). The topographic parameters of the conical island in the model represent an idealization of Dongsha Atoll in the South China Sea (Figure 1a), with a width of 20 km at the flat top, located at a depth of 4 m, and 44 km at the base of the island, situated at a depth of 600 m (Figures 1b and 1d). The island has a constant slope S of 0.05 following the idealized Dongsha Atoll configuration in Rogers et al. (2022). This steep slope is representative of the east side of the Dongsha Atoll in waters shallower than 300 m Fu et al. (2012); Davis et al. (2020). The conical island is surrounded by a domain of constant depth $H = 600$ m. The model domain is 145 km in the x direction (East-West) and 105 km in the y direction (South-North), with 20 km wide sponge layers at the western boundary and periodic boundary conditions at the northern and southern boundaries. The model does not include background currents, even though they have been shown to influence the development of trapped turbulent cores when waves shoal over gentle slopes (Bolioudakis et al., 2026; Lamb, 2003; Lien et al., 2012, 2014). The bottom boundary is characterized by a constant quadratic drag coefficient of $C_D = 0.0025$, while the upper boundary remains a free surface η. Our

model does not include the resolution necessary to capture near bed shear instabilities or turbulent wakes generated when ISWs interact with the seafloor, as documented in high resolution modeling and observational studies (Boegman & Stastna, 2019; Sakai et al., 2020; Trowbridge et al., 2025). These near bed wakes can alter the nature of ISW breaking, including transitions from plunging to collapsing breaking during shoaling, as reported by Aghsaee et al. (2010).

For brevity, we direct readers to the base case in Rogers et al. (2022) for a detailed description of the model setup and island domain layout. Here, we highlight differences from their model settings. The main difference in our model is the forcing. Instead of imposing linear mode-1 internal tides at the eastern boundary, we prescribe velocity and density fields representative of a nonlinear mode-1 ISW obtained from a Dubreil–Jacotin–Long (DJL) solution (Stastna & Lamb, 2002), following the approach of Dunphy et al. (2011). The solution is solely determined by stratification (e.g., buoyancy frequency N_b) and available potential energy. In our simulations, the stratification is based on summer conditions in the northern South China Sea (see Text S2 in Rogers et al. (2022) Supporting Information S1 material) and depth-integrated available potential energy of 18.8 MJ m^{-1} based on observations (Davis et al., 2020; Fu et al., 2012). As a result of the surface-intensified summer stratification, the first baroclinic mode yields an ISW of depression with a maximum isopycnal depression of A_w = 26.4 m, a half wavelength of L_w = 3,194 m, and a wave speed of c = 1.72 m s^{-1} (Figure 1c). These DJL-derived fields are applied as open boundary conditions at the eastern boundary (Fringer et al., 2006). The model reads a NetCDF file every 16 seconds, and values at each intermediate time step are computed by interpolating the DJL fields to the corresponding wave-marching distance based on wave speed (Figure 1c).

Note that the ISWs observed in the South China Sea can reach amplitudes exceeding 150 m (Lien et al., 2014; S. R. Ramp et al., 2004; S. Ramp et al., 2010; S. Ramp et al., 2022). For instance, Cheng et al. (2024) reported a depth-integrated available potential energy of 130 MJ m^{-1} for ISWs near Dongsha Atoll, corresponding to a wave amplitude of approximately 90 m. Despite their larger amplitudes, we argue that these waves would exhibit the same breaker type as those modeled in our study, as they would tend toward a smaller internal Iribarren number. In the Supporting Information S1, we demonstrate that even with deeper shoaling depths, the breaker type and the spatial distribution of the energy budget (see Section 3.2) are consistent with simulations with lower available potential energy (see Figure S3 in Supporting Information S1). However, due to resolution limitations, the model is not able to resolve convective and shear instabilities associated with the shoaling of large-amplitude ISWs (Bolioudakis et al., 2026; Chang et al., 2021). In this paper, we focus our analysis on the lower-energy cases, which offer improved computational efficiency without compromising the generality of the results.

The model grid resolution in both the x and y directions is approximately 50 m around the island and is stretched to 120 m at the domain boundaries. This ensures the resolution of the incident ISW, which requires a horizontal grid resolution at least on the order of the effective depth in order for the model to resolve the leading-order nonhydrostatic dispersion in the ISWs (Vitousek & Fringer, 2011). The vertical grid resolution (Δz) varies exponentially from 2.6 m at the surface to 11.3 m at the maximum depth. A time step of Δt = 8 s, which is based on an internal wave Courant number of $c\Delta t/\Delta x \approx 0.28$, is used to ensure stability of the first-mode internal waves. No attempt was made to parameterize subgrid turbulent mixing processes in the model (i.e., no turbulence model was implemented). Instead, the model employs constant vertical and horizontal kinematic viscosities of $\nu_V = 10^{-3}$ m^2 s^{-1} and $\nu_H = 10^{-1}$m^2 s^{-1}, respectively, with zero vertical and horizontal scalar diffusivities (κ_V and κ_H, respectively). $()_V$ and $()_H$ represent the vertical and horizontal components of a scalar or operator. The choice of constant Laplacian viscosities (ν_V, ν_H) is set by stability requirements related to central differencing for momentum advection rather than to represent actual ocean values. A key component of this study is the inference of depth-integrated dissipation from the energy budget (see Section 2.2), which largely consists of numerical dissipation. Numerical dissipation primarily arises from the numerical diffusion associated with scalar and momentum advection, which becomes more significant where the grid resolution is insufficient to capture sharp gradients, such as beyond the point of wave breaking (Fringer et al., 2005). Although the model does not explicitly simulate turbulent processes associated with dissipation, the areas of elevated numerical dissipation and bottom drag correspond to regions of wave shoaling and breaking, where higher energy losses are expected. Previous studies have shown that the choice of diffusion parameters has only a minor effect on the inferred dissipation (Kang & Fringer, 2012). For a sensitivity test, using a vertical viscosity of $\nu_V = 10^{-4}$ m^2 s^{-1}, the inferred dissipation from the energy budget remains largely unchanged (within 1%). This supports the idea that numerical diffusion plays a more dominant role than the prescribed diffusion, with the former primarily acting on strong

gradients in velocity and tracer fields, much like physical turbulent mixing. The sensitivity test strengthens the argument that explicit turbulence parameterization may not be necessary in this modeling framework. To assess resolution effects, additional two-dimensional simulations (see Section 3.1) at $dx = 25$, 50, and 100 m show that inferred dissipation is similar across runs and decreases with increasing resolution (differences 5%–12%). Higher resolution marginally resolves more overturning, while lower resolution relies more on numerical dissipation to maintain stability. However, we note that methods for directly quantifying local rates of spurious numerical energy dissipation and mixing have been developed (e.g., Griffies et al. (2000); Burchard and Rennau (2008); Ilıcak et al. (2012); Klingbeil et al. (2014)). Although implementing these diagnostics is beyond the scope of the present study, incorporating a direct estimate of numerical energy dissipation is an important next step and will be pursued in future work.

This paper focuses on the energy pathways of a single wave interacting with three-dimensional island topography. Two model runs were conducted in this study. The baseline run involves a single ISW entering the model domain, ending 16 hr after the wave completely passes the island, which takes about 13 hr. The choice of run time is long enough to allow the sponge layer to fully absorb the outgoing wave energy and ensure the relaxation of motions near the island, and short enough to minimize the effects of northern and southern periodic boundaries. The first run ignores the effects of the earth's rotation, while the second run employs rotation by setting the Coriolis parameter at 21°N, the latitude of Dongsha Atoll. The grid size for the runs is $N_x \times N_y \times N_z = 1814 \times 1314 \times 100 \approx$ 238 million points. Running the model for the 29-hr simulation period requires approximately 783,000 time steps. Each simulation, executed in parallel on 400 cores across 10 nodes on the UCI High Performance Community Computing Cluster (HPC3), required roughly 47 hr of wall-clock time.

2.2. Depth-Integrated Energy Budget

To investigate the energy pathways of ISWs interacting with a conical island, we performed a depth-averaged energy budget analysis for both the baroclinic and barotropic energy equations, following Kang and Fringer (2010), which has been applied to wave- and flow-topography interactions in previous studies (Liu et al., 2022; Voet et al., 2023). The incident free-surface mode-1 ISW primarily carries baroclinic energy. A key focus of this analysis is on the conversion between baroclinic and barotropic energy and on the spatial patterns of energy dissipation around the three-dimensional topography of the island.

Let $\langle\rangle = \int_{-h}^{\eta}() \, dz$ be the depth integral of a quantity (), where h and η are bottom depth and free surface elevation, respectively. The horizontal velocity can be decomposed into barotropic and baroclinic components as $\mathbf{u} = \mathbf{U} + \mathbf{u}'$, where $\mathbf{U} = \frac{1}{H}\langle\mathbf{u}\rangle$, and $H = \eta + h$ is the total water depth. The barotropic vertical velocity can be inferred from the continuity equation: $W = -\nabla_H \cdot [(h + z)\mathbf{U_H}]$, and the total vertical velocity can be represented by the sum of the barotropic term and the perturbation term: $w = W + w'$. We assume the density is the sum of a constant reference, depth-dependent background, and disturbance viz. $\rho(x,y,z) = \rho_0 + \rho_b(z) + \rho'(x,y,z)$. The pressure ($p$) is composed of nonhydrostatic (q) and hydrostatic (p_h) components, where $p_h = p_0 + p_b + p' = g\rho_0(\eta - z) + g\int_z^\eta \rho_b \, dz + g\int_z^\eta \rho' \, dz$. The depth-integrated barotropic and baroclinic energy equations are:

$$\frac{\partial}{\partial t}(\langle E_{k0}\rangle + \langle E_{p0}\rangle) + \nabla_H \cdot \langle \mathbf{F}_0\rangle = -\langle C\rangle - \langle \boldsymbol{\epsilon}_0\rangle - D_0, \tag{1}$$

$$\frac{\partial}{\partial t}(\langle E'_k\rangle + \langle E'_p\rangle) + \nabla_H \cdot \langle \mathbf{F}'\rangle = \langle C\rangle - \langle \boldsymbol{\epsilon}'\rangle - D', \tag{2}$$

where $E_{k0} = \frac{1}{2}\rho_0\left(U^2 + V^2\right)$ and $E'_k = \frac{1}{2}\rho_0\left(u'^2 + v'^2 + w^2\right)$ are the horizontal barotropic and total baroclinic kinetic energy densities, respectively. $\langle E_{p0}\rangle = \frac{1}{2}\rho_0 g\eta^2$ is the perturbation potential energy due to surface elevation and $E'_p = \int_{z-\zeta}^{z} g\left[\rho_b(z) + \rho'(z) - \rho_b(z')\right] dz$ is the available potential energy density, where ζ is the vertical displacement of a fluid particle due to fluid motions. $\langle \mathbf{F}_0\rangle$ and $\langle \mathbf{F}'\rangle$ are the depth-integrated horizontal barotropic and total baroclinic energy fluxes:

$$\langle \mathbf{F}_0\rangle = \mathbf{U}_H\langle E_{k0}\rangle + \mathbf{U}_H H\rho_0 g\eta + \mathbf{U}_H\langle p'\rangle + \mathbf{U}_H\langle q\rangle, \tag{3}$$

$$\langle \mathbf{F}'\rangle = \langle \mathbf{u}_H E'_k\rangle + \langle \mathbf{u}'_H E'_{k0}\rangle + \langle \mathbf{u}_H E'_p\rangle + \langle \mathbf{u}'_H p'\rangle + \langle \mathbf{u}'_H q\rangle, \tag{4}$$

where $E'_{k0} = \rho_0(Uu' + Vv')$. D_0 and D' are the bottom drag terms:

$$D_0 = \rho_0 C_d |\mathbf{u}_H|(uU + vV) \text{ at } z = -d, \tag{5}$$

$$D' = \rho_0 C_d |\mathbf{u}_H|\left(uu' + vv' + w^2\right) \text{ at } z = -d. \tag{6}$$

$\langle C \rangle$ is the energy conversion term, which represents the portion of the barotropic energy converted into baroclinic energy or vice versa, that is,

$$\langle C \rangle = \langle \rho' g W \rangle - \langle \frac{\partial q}{\partial z} W \rangle + A_{h0}, \tag{7}$$

where

$$A_{h0} = \rho_0 U \nabla_H \cdot \langle \mathbf{u}'_H u' \rangle + \rho_0 V \nabla_H \cdot \langle \mathbf{u}'_H v' \rangle \tag{8}$$

contains the unclosed horizontal advection terms that first appeared in Kang (2010), but have been neglected in much of the modeling literature estimating surface-to-internal tidal energy conversion, including Kang and Fringer (2012) and Liu et al. (2022). We found that this term is comparable to the hydrostatic pressure work term in shallow regions where the ISW breaks, while the nonhydrostatic pressure work term consistently contributes minimally to the total energy conversion. A positive energy conversion term implies the generation of baroclinic motions due to barotropic forcing, while a negative energy conversion term suggests the emergence of barotropic flow driven by baroclinic processes. Note that the diffusion terms are neglected in (1) and (2) as they are usually several orders of magnitude smaller than other terms, again, following Kang and Fringer (2012).

$\langle \epsilon_0 \rangle$ and $\langle \epsilon' \rangle$ in Equations 1 and 2 are depth-integrated barotropic and baroclinic energy dissipation rates, and their full expression are:

$$\langle \epsilon_0 \rangle = \rho_0 \nu_H H \nabla_H \mathbf{U}_H \cdot \nabla_H \mathbf{U}_H, \tag{9}$$

$$\begin{aligned} \langle \epsilon' \rangle = & \underbrace{\langle \rho_0 \nu_V \frac{\partial \mathbf{u}'_H}{\partial z} \cdot \frac{\partial \mathbf{u}'_H}{\partial z} \rangle + \langle \rho_0 \nu_V \frac{\partial w}{\partial z} \cdot \frac{\partial w}{\partial z} \rangle + \langle \rho_0 \nu_H \nabla_H \mathbf{u}'_H \cdot \nabla_H \mathbf{u}'_H \rangle + \langle \rho_0 \nu_H \nabla_H w \cdot \nabla_H w \rangle}_{\langle \epsilon'_k \rangle} \\ & \underbrace{+ \langle g \kappa_H \nabla_H \rho' \cdot \nabla_H \zeta \rangle + \langle g \kappa_V \frac{\partial (\rho_b + \rho')}{\partial z} \frac{\partial \zeta}{\partial z} \rangle}_{\langle \epsilon'_p \rangle}, \end{aligned} \tag{10}$$

where ν and κ are the eddy viscosity and eddy diffusivity, respectively. Since turbulent processes are not explicitly resolved at the model resolution used here, numerical dissipation is diagnosed by inferring the depth-integrated energy dissipation by summing (1) and (2):

$$\langle \boldsymbol{\epsilon} \rangle \approx -\frac{\partial}{\partial t}(\langle E_{k0} \rangle + \langle E_{p0} \rangle) - \frac{\partial}{\partial t}(\langle E'_k \rangle + \langle E'_p \rangle) - \nabla_H \cdot \langle \mathbf{F}' \rangle - \nabla_H \cdot \langle \mathbf{F}_0 \rangle - D_0 - D', \tag{11}$$

where the positive and negative energy conversion terms cancel out.

3. Results and Discussion

3.1. ISW Shoaling, Breaking, and Reflection

The incident wave of depression is introduced progressively over time at the eastern boundary of the model and propagates westward, interacting with the conical island after $t = 5.15$ wave periods, where a wave period is defined as $2L_w/c \approx 1$ hr. The Iribarren number $I_r = \frac{S}{\sqrt{A_w/L_w}}$ (ratio of the bottom slope to the slope of the incident wave) can be an useful indicator for predicting ISW breaking characteristics on sloping bathymetry (Aghsaee et al., 2010; Boegman et al., 2005; Sutherland et al., 2013). For example, Boegman et al. (2005) found that an ISW

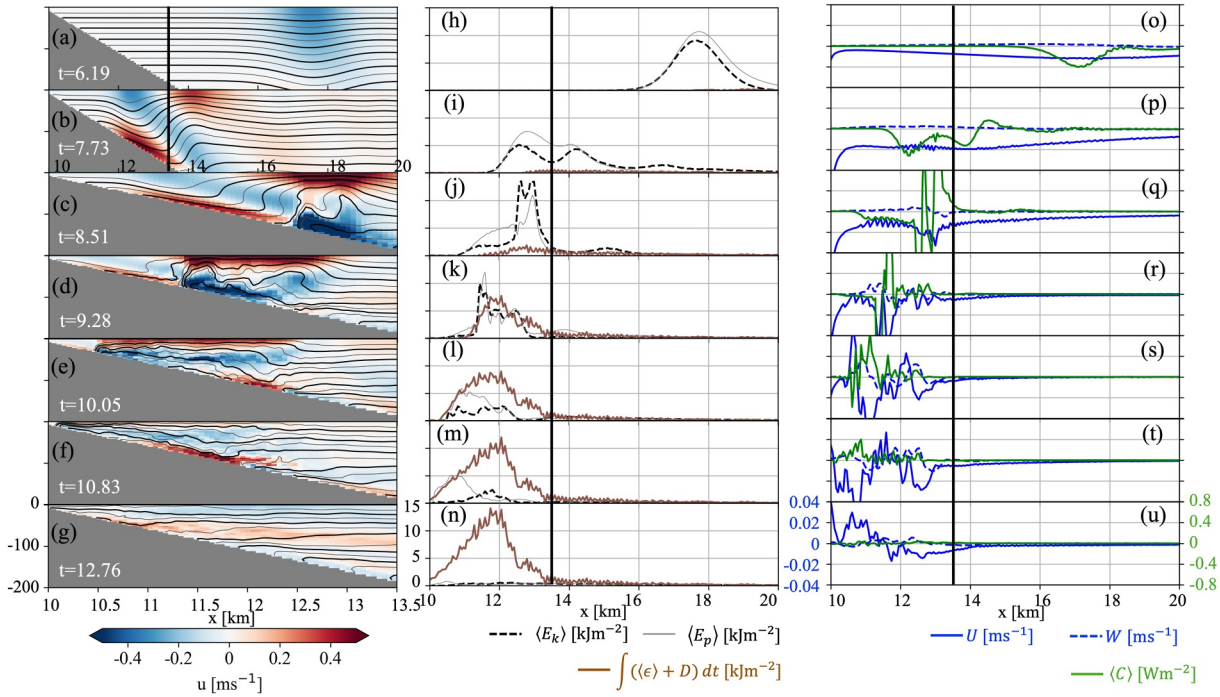

Figure 2. In the no-rotation case, the time evolution of the incident internal solitary wave (ISW) is shown in (a–g) along the transect on the eastern slope of the island (black line in Figure 1b). Panels (c–g) show isopycnals and along-transect velocities with enhanced horizontal zoom to highlight wave shoaling and breaking. The middle column (h–n) shows the total depth-integrated kinetic and potential energy (the sum of barotropic and baroclinic components) and the sum of the time-integrated depth-integrated dissipation and bottom drag. The vertical black lines indicate a shoaling depth of 180 m, above which the breaking of the shoaling ISW transfers wave energy into dissipation. The right column (o–u) shows the barotropic horizontal velocity, barotropic vertical velocity, and the depth-integrated energy conversion term.

described by Korteweg-de Vries theory forms plunging breakers when $0.45 < I_r < 0.75$. For an island slope of $S = 0.05$ in our model setting, $I_r = 0.55$ suggests a plunging breaker type, consistent with the findings for large amplitude ISWs in Aghsaee et al. (2010) and Sutherland et al. (2013). As the ISW shoals up onto the eastern slope of the island (see transect in Figure 1b), it steepens at the back (Figures 2b–2d), forming a wave of elevation that becomes gravitationally unstable (Figure 2d), characteristic of a plunging breaker. Plunging breakers drive the most effective mixing among all breaker types (Boegman & Ivey, 2009). The shoaling, polarity change, and breaking of ISWs have been documented through observations from a mooring array deployed over a slope similar to the model configuration ($S = 0.052$) east of Dongsha Atoll, as reported by Fu et al. (2012) and Sinnett et al. (2022). The leading edge of the wave of depression interacts with the sloping topography, causing strong downslope flow near the seabed (Figures 2b–2e). This feature, that is, the "internal rundown", has been found on the eastern slope of Dongsha Atoll using a bottom-mounted DTS system (Davis et al., 2020). After breaking occurs, a turbulent bore of dense water runs up the shallow slope (Figures 2d–2f) until it loses its onshore momentum and relaxes offshore (Figure 2g).

The kinetic energy of a freely propagating ISW is always greater than the available potential energy (Lamb & Nguyen, 2009) (e.g., before the incident wave reaches the island slope, not shown in Figure 2). As the wave shoals onto shallow slopes, it decelerates, leading to a conversion of kinetic energy into available potential energy (Figures 2h–2j). Upon breaking in even shallower waters, both kinetic energy and available potential energy decrease as energy dissipates through turbulent mixing and bottom friction (Figures 2k–2n). Based on visual inspection, we estimate that the incident shoaling ISW begins to break at a depth of approximately 180 m on the eastern slope of the island. The majority of dissipation occurs at shallower depths (black lines in Figure 2). We refer to this depth as the "shoaling depth", which is conceptually similar to the "saturation depth" described in Becherer et al. (2021a, 2021b), beyond which the available potential energy of the internal wave must decrease due to water depth limitations, as well as the "maximum interface descent" for a two-layer breaking ISW, $\sqrt{4SA_wL_w}$, proposed in Sutherland et al. (2013). The model-inferred "shoaling depth" aligns well with observations made at Dongsha Atoll (Davis et al., 2020; Fu et al., 2012). For comparison, the "maximum interface

descent" proposed by Sutherland et al. (2013) is estimated to be 130 m. While this is shallower than the shoaling depth, it corresponds well with the location of maximum dissipation. Similarly, the estimated "saturation depth" based on Equation 15 in (Becherer et al., 2021b) is also relatively shallow, at around 60 m, suggesting that energy dissipation occurs before the wave energy becomes saturated, or that the parameterization may need to be fine-tuned to better represent three-dimensional topography and/or incident nonlinear internal waves in this study.

In addition to the shoaling and breaking of the incident ISW on slopes in shallow waters, reflection or partial reflection can also occur (Bourgault & Kelley, 2007; Lamb & Nguyen, 2009). A measure of wave reflection is the reflectance coefficient R, typically evaluated near the base of the topographic slope, by dividing the reflected energy flux by the incident ISW energy flux (Lamb & Nguyen, 2009; Shepherd, 1993). The reflectance coefficient R ranges between zero and one, increasing with the Iribarren number. On very steep topographic slopes, the wave reflects without breaking ($R \to 1$), while on very shallow slopes, there is little reflection and the wave breaks and dissipates its energy instead of reflecting ($R \to 0$). A parameterization for R proposed by Bourgault and Kelley (2007), $R = 1 - e^{-I_r/0.78}$, demonstrates the dependence of reflectance on the Iribarren number. This parameterization was found to fit well with high-resolution two-dimensional simulations when applied before the shoaling and breaking point, beyond which energy dissipation occurs (Aghsaee et al., 2010). Using the I_r from the model, the Bourgault and Kelley (2007) parameterization predicts $R = 0.5$. We calculate the energy fluxes in the radial direction and determine the reflectance along the eastern foot of the island (blue transect in Figure 1b) by dividing the time- and depth-integrated offshore energy flux by the onshore flux. Reflectance (R) along transects farther from the island (Figures S1 and S2 in Supporting Information S1) shows similar patterns but with smaller amplitudes compared to those calculated at the island foot. We found that reflectance varies around the island, being around 0.18 on the eastern side and increasing toward the northern and southern sides of the island (solid curve in Figure 3), with values smaller than that predicted using the formula from Bourgault and Kelley (2007). This may be due to the fact that the parameterization was based on effective two-layer ISWs, whereas the ISWs in our model are generated under surface-intensified but continuous stratification. The variation along the eastern foot of the island results from the misalignment between the wave rays and the radial coordinates due to wave refraction, as well as the complex energy advection toward the northern and southern sides of the island (Figure 4). In the rotation run, however, an asymmetry in reflectance is caused by a shift in the location of the wave rays (dashed curve in Figure 3). The reflectance reaches approximately 0.14 on the eastern side of the island. For comparison, previous studies at Dongsha Atoll observed that approximately 20% of the incident wave energy is reflected at sites east of the atoll (Bai et al., 2017; Davis et al., 2020).

3.2. Spatial Distribution of ISW Energy Fluxes

As discussed in the previous section, the literature on internal wave energetics on a slope has been restricted to two-dimensional topography, wherein incident ISW energy at a two-dimensional slope typically involves partial reflection and partial transmission across the slope, where it eventually dissipates due to mixing induced by wave breaking. These dynamics are largely dictated by the relationship between the ISW slope and the topographic slope (i.e., the Iribarren number). Our simulations indicate that the fate of incident ISW energy in the three-dimensional island is more complex, as the wave shoals, refracts, and energy is fluxed along slope as well as across slope. Thus, the spatial distribution of energy dissipation depends to a great extent on the angle of incidence between the ISW and the topographic slope. Wave shoaling and breaking can occur not only on the eastern slope of the island (i.e., directly incident side) but also on its flanks and western slope. Furthermore, the baroclinic energy of the incident wave is partially converted into barotropic energy, which not only contributes to the reflectance but can also propagate around the island. To further understand the energetics of the shoaling and breaking ISW over three-dimensional sloping topography, we evaluated the time- and depth-integrated baroclinic and barotropic energy fluxes, as well as the energy conversion, bottom drag, and inferred dissipation terms in the energy budget (Equations 1 and 2). The time-integrated unsteady terms in Equations 1 and 2—i.e., the differences in kinetic and potential energy between the start time ($t = 0$) and the end time ($t = 29$)—are negligible (as shown by the near-zero values of $\langle E_k \rangle$ and $\langle E_p \rangle$ at $t = 12.76$ in Figure 2n). This indicates a relaxation of the wave–topography interaction and minimal influence from reflected waves at the model boundaries.

Figures 4a and 4b show that the westward baroclinic energy flux is redirected around the island and onshore over shallow slopes due to wave refraction. A significant reduction in baroclinic energy flux occurs from east to west of the island. For example, the no-rotation run shows that the westward time-integrated baroclinic energy flux along

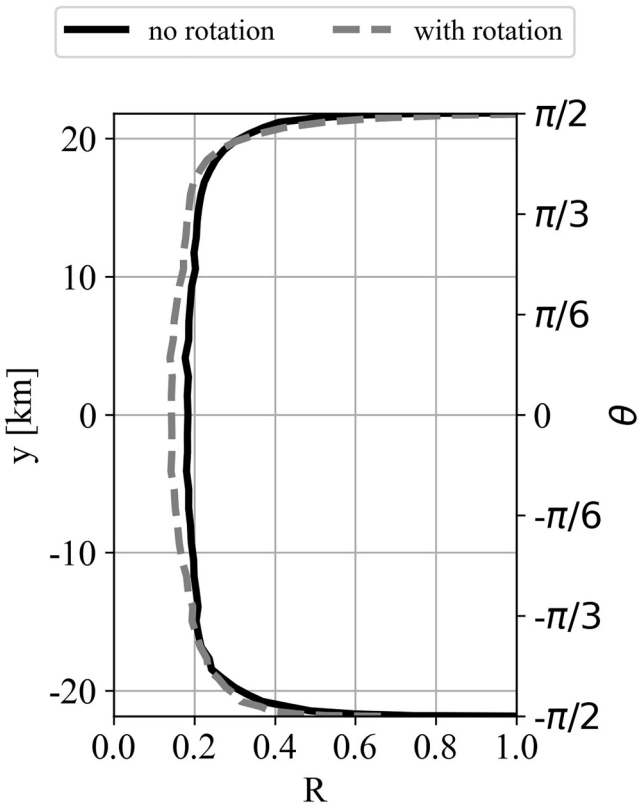

Figure 3. The influence of rotation on the reflectance calculated along the foot of the island (see the blue transect in Figure 1b). Here, $y = 0$ and $\theta = 0$ correspond to the eastern side of the island, where the internal solitary wave is normally incident; positive y and θ indicate counterclockwise directions around the island. The island spans approximately $y = \pm 21.8$ km, with $y = 21.8$ km (or $\theta = \pi/2$) marking the northern tip and $y = -21.8$ km (or $\theta = -\pi/2$) marking the southern tip.

the western section ($x = -40$ km) over the island range, with a latitudinally averaged flux of 10 MJ m^{-1}, is only about 27% of the flux over the same range along the eastern section ($x = 40$ km), which has a latitudinally averaged flux of 36 MJ m^{-1}. This indicates that approximately 73% of the unreflected incident ISW energy flux over the island range was lost to dissipation and bottom friction. Recall that the reflectance is around 20% over the eastern slopes. This suggests that 58% of the incident ISW energy is dissipated within the island region, while only 22% passes beyond the island. Over the island, 85% of the total energy dissipation is concentrated in areas shallower than the shoaling depth, where the wave shoals and breaks, while only 15% occurs over the deeper slopes. Bottom drag accounts for just 15% of the total dissipation in these shallow regions, compared to about 54% over deeper slopes.

The incident wave is generated at the eastern boundary as a solution to the rigid-lid DJL equation. It initially contains only baroclinic energy. As the wave propagates toward the island, the free-surface model allows it to adjust dynamically. The energy remains predominantly baroclinic. This is evident from the baroclinic energy flux vectors directed toward the island from the eastern basin, with no observable barotropic flux (Figure 4). However, barotropic energy fluxes develop near the island's slopes. This suggests that the interaction of the ISW with the island slopes causes baroclinic to barotropic energy conversion ($\langle C \rangle < 0$). As shown in Figures 4c and 4d, baroclinic-to-barotropic energy conversion occurs over the entire slope on the eastern side of the island and over areas shallower than the shoaling depth on its northern and southern flanks. Barotropic-to-baroclinic energy conversion, however, occurs over island slopes deeper than the shoaling depth on the northern, southern, and western sides of the island.

To quantify the spatial heterogeneity of ISW energy around the island, we integrate the energy budget within four quadrants (Figure 5). Each quadrant is further divided into inner and outer quadrants by the 180 m isobath (i.e., the shoaling depth). We find that, of the 85% of total energy dissipation concentrated in areas shallower than the shoaling depth, approximately half occurs in the inner eastern quadrant. The inner northern and southern quadrants each account for slightly less than a quarter of the total dissipation (east: 46.7%, north and south: 23.7%, west: 5.9%). The inclusion of Earth's rotation results in a north-south asymmetry, with ≈3% more dissipation in the inner northern quadrant than in the inner southern quadrant (east: 47.2%, north: 25.0%, south: 22.3%, west: 5.5%). We can estimate the depth-integrated dissipation rate by dividing the time- and volume-integrated dissipation within different quadrants by the area and the M2 tidal period (T_{M2} =12.42 hr), consistent with the internal wave period observed in the South China Sea (S. Ramp et al., 2010; Zhang et al., 2011). The estimated dissipation rates in the inner quadrants (average of 3×10^{-2} W m^{-2} across all quadrants) are comparable to observations from the continental shelf of the South China Sea near Dongsha Atoll (5×10^{-2} W m^{-2}; St. Laurent (2008)). The average rate in the eastern inner quadrant is approximately twice as large (see Tables S1 and S2 in Supporting Information S1).

Baroclinic energy flux convergence and barotropic energy flux divergence are found in the eastern quadrants and the inner northern and southern quadrants, corresponding to the baroclinic-to-barotropic energy conversion. In contrast, baroclinic energy flux divergence and barotropic energy flux convergence are found in the northern, southern, and western outer quadrants, corresponding to the barotropic-to-baroclinic energy conversion. The area-integrated energy conversion is typically one to two orders of magnitude smaller than the dissipation in regions shallower than the shoaling depth but is of the same order of magnitude in deeper regions. This distinction highlights different energy pathways over the shallower and deeper island slopes, with the former dominated by dissipation and the latter involving both dissipation and conversion. Over the entire island slopes, baroclinic-to-barotropic energy conversion accounts for 20% of the total divergence of baroclinic energy flux. This converted

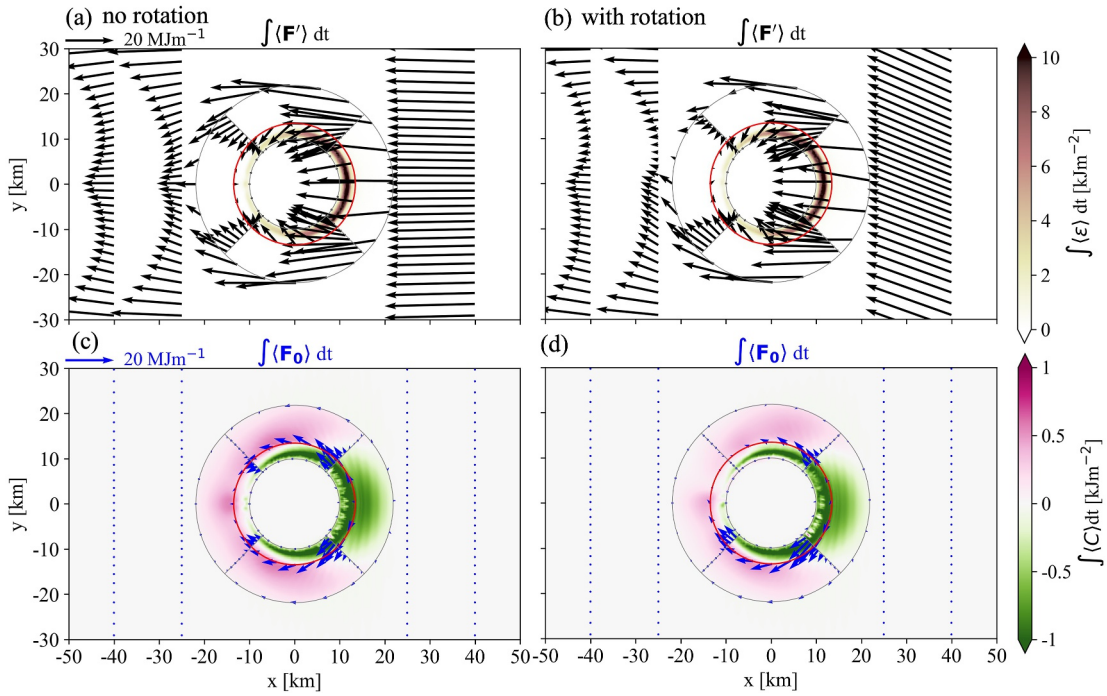

Figure 4. (a), (b) Time- and depth-integrated baroclinic energy fluxes along selected meridional sections eastward and westward of the island, the shoaling depth (red circle), the foot of the island, and the quadrants divisions are shown with black arrows, while the dissipation is represented by colors. (c), (d) Time- and depth-integrated barotropic energy fluxes (blue arrows) and baroclinic-barotropic energy conversion (colors). Negative values indicate baroclinic-to-barotropic conversion, and positive values indicate barotropic-to-baroclinic conversion. Note that the incident wave contains primarily baroclinic energy. (a), (c) and (b), (d) correspond to the no-rotation and with-rotation runs, respectively.

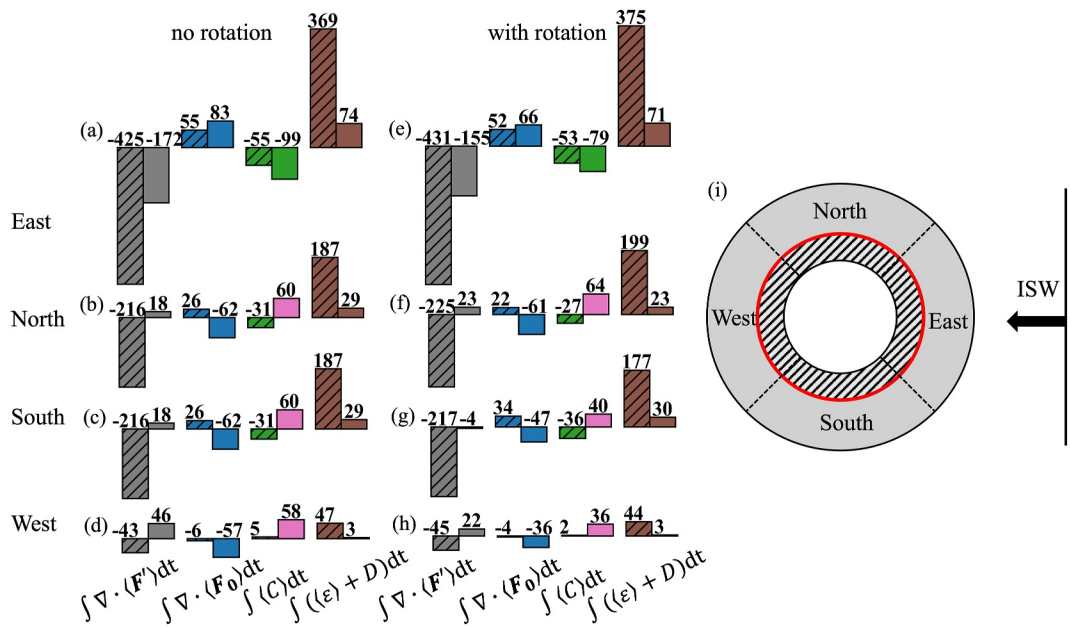

Figure 5. Time- and depth-integrated energy budget terms (in units of GJ) — including baroclinic energy flux divergence $\int\nabla\cdot\langle F'\rangle dt$ (gray), barotropic energy flux divergence $\int\nabla\cdot\langle F_0\rangle dt$ (blue), energy conversion $\int\langle C\rangle dt$ (positive for baroclinic-to-barotropic conversion: pink; negative for baroclinic-to-barotropic conversion: green), and the sum of inferred dissipation and bottom drag (brown) $\int(\langle\epsilon\rangle + D)dt$ — area-integrated within four quadrants and further divided into inner and outer quadrants by shoaling depth (red circle in i; 180 m). (a–d) and (e–h) correspond to the no-rotation and with-rotation runs, respectively. Hatched areas are shallower than the shoaling depth.

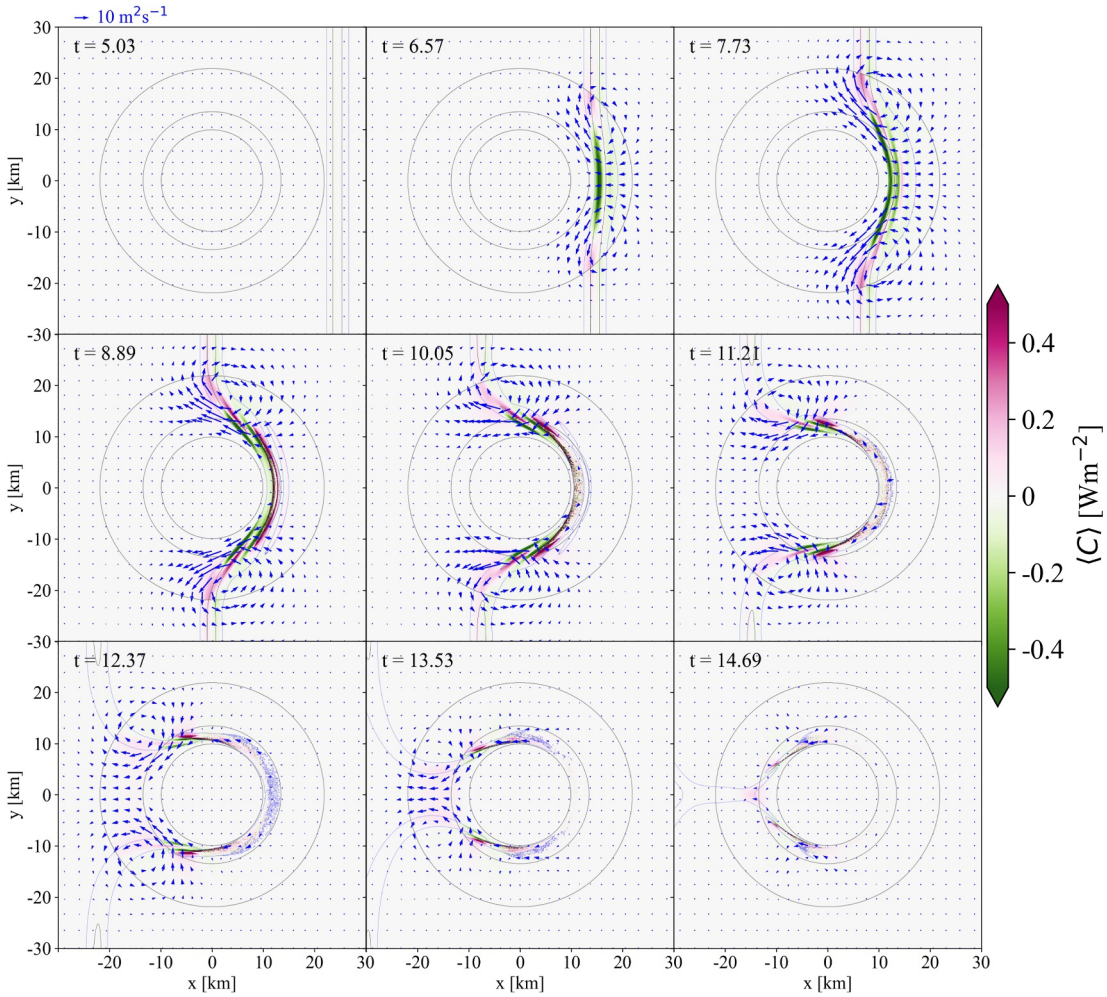

Figure 6. Time evolution of depth-integrated energy conversion (color shading) and depth-integrated barotropic velocities (blue vectors) is shown for the no-rotation run. Gray contours of baroclinic energy delineate the time evolution of wave crests. Negative energy conversion (green) indicates baroclinic-to-barotropic energy transfer, while positive energy conversion (pink) represents barotropic-to-baroclinic transfer.

energy is eventually balanced by barotropic-to-baroclinic energy conversion, which transfers energy back to baroclinic waves before it is dissipated.

3.3. Baroclinic-to-Barotropic Energy Conversion of Shoaling ISWs

The baroclinic-to-barotropic energy conversion over the eastern slopes of the conical island is associated with the interaction of the ISW with the sloping topography. This is of particular interest, given that most studies typically report barotropic-to-baroclinic energy conversion that arises when internal tides are generated by barotropic tidal flow over topography (e.g., Kang and Fringer (2012)). Such studies typically attribute negative conversion to a phase difference between locally- and remotely generated internal waves (Zilberman et al., 2009).

In our model, as the ISW propagates into the sloping island topography from the east, the change in topography induces a positive barotropic vertical velocity W (Figures 2a, 2b, 2o and 2p). Baroclinic kinetic energy is partially converted to barotropic kinetic energy through pressure work by barotropic vertical movement $\langle \rho' g W \rangle$, resulting in a net positive barotropic energy flux divergence over the eastern slope of the island (Figure 5a). Barotropic-to-baroclinic energy conversion appears at the rear of the steepening wave as it transitions into a wave of elevation (Figures 2c, 2d, 2q and 2r). As the rear of the wave becomes gravitationally unstable and breaks, the barotropic flow changes direction intermittently. The energy conversion appears to be primarily from barotropic to

baroclinic (Figures 2e, 2f, 2s and 2t). As the wave passes the slope, the energy conversion returns to near zero (Figures 2g and 2u).

Figure 6 shows the temporal evolution of the energy conversion term throughout the internal wave interaction with the island, as well as the evolution of wave crests. The wave crests are indicated by the depth-integrated total baroclinic energy ($\langle E_k' \rangle + \langle E_p' \rangle$). Baroclinic-to-barotropic energy conversion first occurs on the eastern slopes of the island, following the crest of the shoaling ISW ($t = 6.57$). This leads to the emergence of onshore barotropic flow in the same region. The transient barotropic flow forms a pair of recirculation regions that propagate along the island slopes, following the wave crest, and eventually converges on the western side of the island ($t = 6.57$–14.69). Following the wave crest, baroclinic-to-barotropic energy conversion also occurs on the shallow slopes of the island flanks and western side.

Within the recirculation regions, the barotropic volume flux is directed downslope in the leading edge and upslope in the trailing edge of the wave. Barotropic-to-baroclinic energy conversion occurs near the leading edge of the wave (i.e., on the downslope), coinciding with the convergence of the downslope-directed barotropic energy flux. This energy transfer may be estimated using theory for lee wave generation, which extracts energy from the barotropic flow. An estimate of the conversion from a quasi-steady flow to lee wave energy, based on Miles and Huppert (1969) and Bell Jr (1975), is given in units of W m^{-1} by $\frac{\pi}{8}\rho_0 U_0^2 h_0^2 N$. This estimate applies to flow over a smooth hill shape known as the "Witch of Agnesi", assuming no rotation. We estimate the conversion to lee wave energy using typical values from the recirculation region at time $t = 8.89$. These include a barotropic velocity of $U_0 = 0.05$ m s^{-1}, a bathymetry height of $h_0 = 400$ m at the inner edge of the vortices, a surface buoyancy frequency of $N = 10^{-3}$ s^{-1}, and a background density of $\rho_0 = 10^3$ kgm^{-3}. We assume the energy conversion occurs over a distance of about half a wavelength, estimated as $L_w = 3$ km. Dividing the total conversion by this distance gives an energy conversion rate of roughly 0.1 W/m^2, which is similar in magnitude to what we see in the model results. Barotropic recirculation cells and similar patterns of baroclinic-barotropic energy conversion are also found in the rotation run, albeit with some north–south asymmetry (Figure S4 in Supporting Information S1).

3.4. Role of Three-Dimensional Topography on ISW Energy Pathways

Here we examine the energetics of ISWs shoaling on three-dimensional topography compared to the better-studied, two-dimensional case. For comparison to the three-dimensional simulation with no rotation described above, we conducted a two-dimensional model run without rotation, incorporating a uniform topographic slope with a flat slope top and a deep basin to the east. Periodic boundary conditions were applied to the northern and southern boundaries, simulating an infinitely long two-dimensional slope. The slope configuration matches the eastern slope of the conical island in the three-dimensional simulations. The model resolution, background stratification, and incident ISW at the eastern boundary are identical between the two setups. In both runs, the incident ISW takes the same amount of time to reach the slope. The model was run until the area- and depth-integrated total energy over the slope approached zero, and the time-integrated dissipation reached a constant value.

In the two-dimensional slope simulation, the incident ISW shoals and breaks at depths similar to those in the three-dimensional island simulation, producing dissipation that is of the same order as that on the eastern slopes of the conical island (Figure S5 in Supporting Information S1). We further estimated the time-integrated energy terms averaged over the entire slope in the two-dimensional run and over the eastern quadrant slope in the three-dimensional run (Figure 7). The baroclinic-to-barotropic energy conversion averaged over the two-dimensional slope is negligible compared to that over the conical island slopes in the three-dimensional case. Consequently, barotropic energy is negligible in the two-dimensional simulation. A comparison of the time evolution of depth-integrated energy fluxes, barotropic velocities, and energy conversion is provided in Figures S6, S7, and S8 in Supporting Information S1. These results consistently indicate that the two-dimensional topographic slope does not induce significant transient barotropic–baroclinic energy conversion, resulting in negligible barotropic flows and energy fluxes.

The incident nonlinear ISW of depression is characterized by a positive surface elevation and a negative dynamic height with a reference level at the bottom, due to its baroclinicity (Figure 8c). In both the three-dimensional and two-dimensional simulations, as the ISW shoals over the slope, it induces a surface elevation build-up over the shallower regions, which resembles the "set-up" within the surf zone caused by shoaling and breaking surface

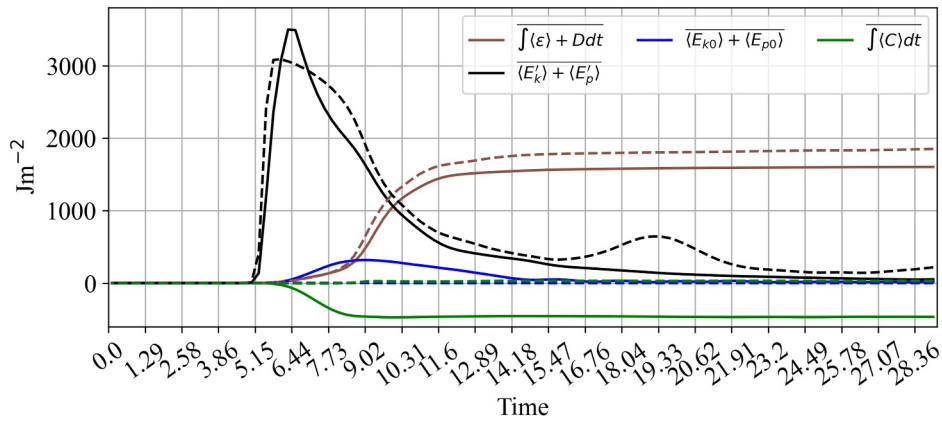

Figure 7. Depth-integrated total baroclinic $\langle E'_p\rangle + \langle E'_k\rangle$ and barotropic energy $\langle E_{p0}\rangle + \langle E_{k0}\rangle$, along with time- and depth-integrated total dissipation $\langle\epsilon\rangle + D$ and energy conversion $\langle C\rangle$, averaged over the entire eastern quadrant slopes for the three-dimensional island simulation (solid lines), and over the entire slope for the two-dimensional slope simulation (dashed lines).

waves (Bowen et al., 1968) (Figures 8a, 8b and 8d). Here, we acknowledge that the surface wave "set-up" is a time-averaged phenomenon occurring over multiple wave cycles, whereas the model simulates the shoaling of a single wave over a topographic slope. We refer to the term only in relation to its inshore surface height build-up feature, rather than its full physical interpretation. Furthermore, the curved coastline in the three-dimensional island setting also allows this "set-up" to develop in the alongshore direction, as shown in Figures 8d and 8e, where the onshore sea surface elevation exhibits a gradient in the y-direction. Although the dynamic height field does not show the "set-up" response seen in the surface elevation, it does exhibit a gradient in the y-direction. The barotropic pressure gradient from both components enables barotropic flow to develop in both the cross- and longshore directions. The onshore barotropic velocity is balanced by a longshore component directed away from the eastern slope (Figures 8d and 8e), leading to the formation of recirculation regions in the depth-averaged flow (Figure 8a). In contrast, a longshore sea surface elevation gradient does not form in a two-dimensional slope or in

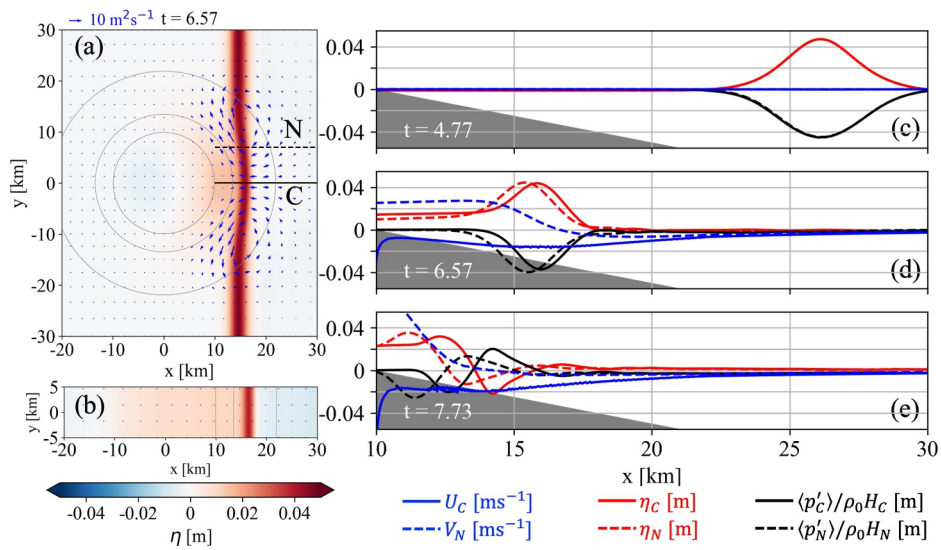

Figure 8. Surface elevation η and depth-integrated barotropic velocities for the no-rotation three-dimensional island simulation (a) and the two-dimensional slope simulation (b). Gray contours mark the slope top, shoaling depth (defined from the three-dimensional simulation), and the foot of the slope. (c)–(e) Time snapshots show the development of barotropic velocities in the x (U) and y (V) directions, associated with along-slope variations in surface elevation η and depth-integrated dynamic height $\langle p'\rangle/\rho_0 H$ in the three-dimensional run. Variables along the north (N) and center (C) sections, as indicated by the subscripts and marked in (a), are shown using dashed and solid lines, respectively.

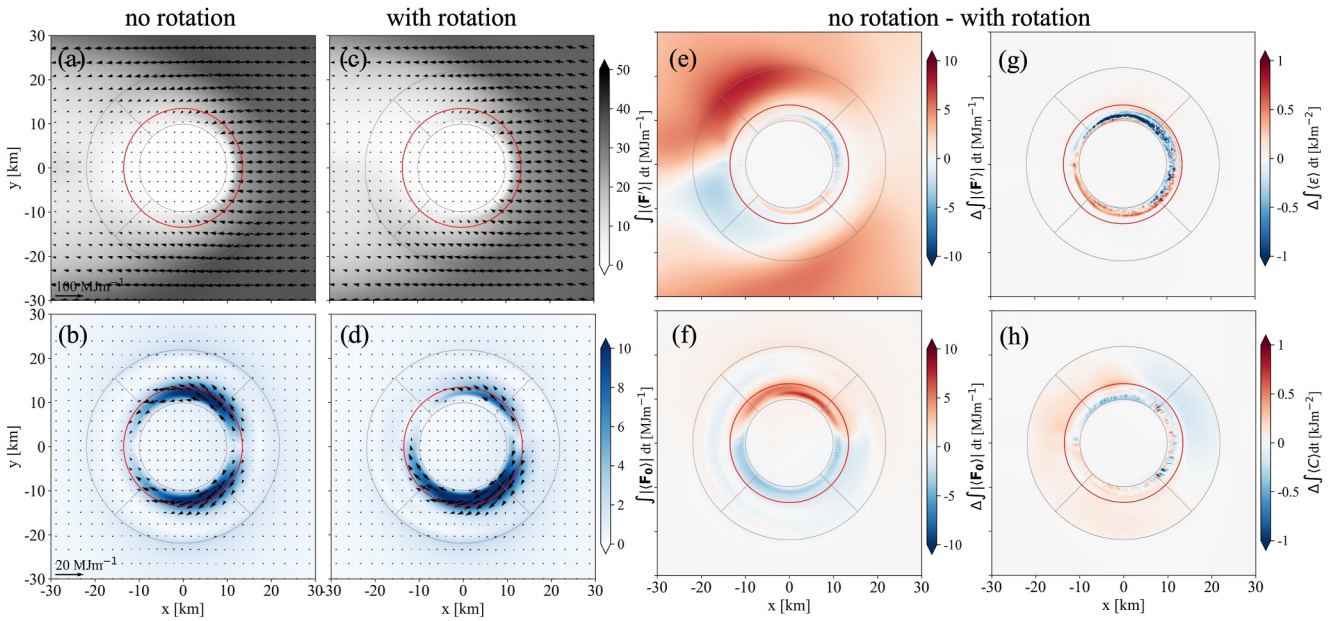

Figure 9. Time- and depth-integrated baroclinic and barotropic energy fluxes for runs without (a), (b) and with (c), (d) rotation, respectively. The differences between the two runs are shown for time- and depth-integrated baroclinic (e) and barotropic (f) energy fluxes, dissipation (g), and energy conversion (h).

the case of a normally incident wave interacting with a straight coastline (Figure 8b). As a result, barotropic flow cannot develop in the longshore direction, which is reflected by the negligible baroclinic-to-barotropic energy conversion, as shown in Figure 7b.

3.5. Role of Rotation in Shoaling ISWs

Comparison between the no-rotation and with-rotation runs highlights the influence of the Earth's rotation on ISWs. Coriolis dispersion tends to counteract the steepening effect of nonlinearity, which can reduce the amplitude or even destroy the ISW by the radiation of small-amplitude inertia–gravity (Poincaré) waves (R. H. Grimshaw et al., 1998) and may form a secondary trailing wave packet via steepening (Helfrich, 2007; R. Grimshaw et al., 2014; Lamb & Warn-Varnas, 2015). In this study, the Coriolis force affects the incident wave as it propagates from the eastern boundary of the model domain to the island. However, these processes have limited impact on wave propagation in our study, as they occur over time scales longer than the inertial time period of 31 hr ($t \approx 31$) (Farmer et al., 2011). This exceeds both the total simulation duration of 29 hr and the approximately 10-hr window during which the ISW interacts with the island. However, Coriolis dispersion causes small waves to emerge behind the incident ISW and energy fluxes appear in the direction transverse to the ISW propagation direction (Figure S9 in Supporting Information S1). If the upstream basin had been long enough, we suspect that a trailing wave packet could have fully developed. As a result of this wave radiation, the peak incident wave energy entering the island slope from the east is slightly lower (by 7%) in the rotation run compared to the no-rotation run.

The time- and depth-integrated energy budgets from the baseline and rotation runs indicate that the Coriolis force plays a key role in modulating the spatial distribution of energy pathways over the island slopes (Figure 9). Rotation alters the direction of the baroclinic energy flux of the incident ISW, shifting the pattern clockwise. This shift results in reduced baroclinic energy flux over the northeastern slopes within the shoaling depth and enhanced flux over the southeastern slopes (Figures 9a– 9c and 9e). Since convergence of the baroclinic energy flux leads to dissipation, the rotation run exhibits higher dissipation over the northern slope compared to the southern slope (Figure 9g; Tables S1, S2 in Supporting Information S1).

The barotropic energy flux is concentrated in regions shallower than and around the shoaling depth due to its convergence over deeper slopes (Figures 9b and 9d). Similarly, the Coriolis force shifts the barotropic energy flux clockwise, while also reducing the flux over the northern slopes and intensifying the flux over the southern slopes

(Figure 9f), which corresponds to changes in the energy conversion patterns (Figure 9h). This effect is also evident in the barotropic recirculation cells caused by energy extraction from the shoaling and breaking ISW (Figure S4 in Supporting Information S1), with stronger barotropic velocities in the southern cell compared to the northern cell.

4. Summary

In this study, we conducted idealized numerical simulations of an ISW shoaling and breaking at a conical island, representing ISWs interacting with the Dongsha Atoll in the South China Sea. To better understand the fate of the incident ISW over three-dimensional topography, we conducted a detailed energy budget analysis. This analysis focused on the spatial patterns of wave energetics around the conical island and the pathways of ISW energy, including energy dissipation and the conversion between baroclinic and barotropic energy components. Our results show that within the range of the island, around 20% of the incident ISW energy is reflected along the eastern slopes, 58% is dissipated within the island, and only 22% passes beyond it. Over the entire island slopes, approximately 85% of total energy dissipation (i.e., summation of dissipation and bottom drag) occurs in regions shallower than the shoaling depth, marked by the 180 m isobath, where the wave shoals and breaks. The spatial distribution of total dissipation over these shallow slopes is heterogeneous, with roughly half occurring on the island's eastern slope. About one-quarter of the dissipation takes place along each of the northern and southern flanks, while only a small fraction is located on the western side. Approximately 20% of the baroclinic energy flux divergence is converted into barotropic energy flux by generating a transient baroclinic flow, which subsequently reconverts its energy into baroclinic waves before eventually dissipating, highlighting a potentially important energy pathway.

As the incident wave steepens and shoals over the island slopes, baroclinic energy is partially converted into barotropic energy. The interaction between the ISW and the three-dimensional topography allows longshore pressure gradients, which arise from surface setup and dynamic height, to generate transient barotropic flows. In contrast, a two-dimensional slope under the same wave forcing shows negligible energy conversion. The converted barotropic energy generates a pair of barotropic recirculation regions that travel along the island slopes with the wave. Downslope and upslope barotropic velocities develop at the leading and trailing edges of these recirculation regions, respectively. Barotropic-to-baroclinic energy conversion occurs primarily at the leading edge, where the barotropic energy flux is directed downslope—a process that may resemble the generation of baroclinic lee waves by barotropic flow. As a result, the spatial distribution of energy conversion exhibits heterogeneity, with baroclinic-to-barotropic energy conversion occurring on the eastern slopes and shallow areas of the island's flanks, while barotropic-to-baroclinic energy conversion is found on the deeper slopes of the flanks and the western side of the island. Earth's rotation influences the spatial patterns of energy fluxes, energy conversion, and dissipation around the island. In the Northern Hemisphere setting of Dongsha Atoll, the fluxes shift clockwise, with intensified dissipation occurring in the northern part of the island and ISW-generated barotropic flow strengthening along the southern slopes.

This study highlights the spatial heterogeneity of dissipation and a distinctive pathway of energy transfer from baroclinic to barotropic energy during ISW interactions with three-dimensional topography. Three-dimensional topography supports barotropic energy fluxes that are transverse to the incident ISW baroclinic energy fluxes, a complexity not fully captured by two-dimensional parameterizations relying solely on energy flux convergence in the cross-shore direction. Furthermore, high dissipation is found not only on the eastern slope of the island, where the ISW first interacts with the island, but also across the adjacent flanks. The findings emphasize the critical need for spatially distributed observations of internal wave energetics over three-dimensional topography to improve our understanding of these processes. Such efforts are vital for advancing knowledge of the biological and ecological impacts on local marine communities, including coral reefs.

We note that the present study focuses on the energetics and barotropic-baroclinic energy transformations associated with an ISW shoaling into a plunging breaker over a steep slope. The chosen topographic slope ($S = 0.05$) is representative of the eastern flank of Dongsha Atoll but is considerably steeper than the continental slope in the northern South China Sea, where typical slopes range from 0.01 to 0.02. Over these gentler slopes, large-amplitude ISWs of O(100–200 m) have been observed to undergo internal breaking well before reaching the steep topography of the atoll (Lien et al., 2012, 2014). During this stage, ISWs may develop a highly turbulent subsurface trapped core and experience both convective and shear instabilities while still maintaining an overall

solitary-wave structure over several wavelengths. Such behavior has been documented in field observations over the northern South China Sea continental slope (Chang et al., 2021; Lien et al., 2012, 2014) and reproduced by recent field-scale, turbulence-resolving simulations (Bolioudakis et al., 2026) that leverage a nonhydrostatic spectral-element framework (Diamantopoulos et al., 2022). This internal breaking and trapped-core formation may also trigger fission processes, leading the ISW to separate into a large primary wave followed by slower trailing secondary waves (Lien et al., 2012; S. R. Ramp et al., 2004).

In contrast, our model prescribes a constant conical-island slope within a deep basin of uniform depth, such that the incident ISW does not undergo this gentler-slope internal breaking prior to shoaling. This configuration allows us to isolate the dynamics of the steep-slope plunging breaker. Because the convective and shear instabilities that occur over gentle slopes can produce substantially different magnitudes and spatial patterns of turbulent mixing and kinetic energy dissipation, the resulting breaking behavior and barotropic–baroclinic energy exchange likely differ from the dynamics examined here. Although gentler-slope breaking pathways are not addressed in the present study, their influence on ISW energetics represents a valuable direction for future research. Additionally, the bending of the wave crests along the island slopes arises from wave refraction, and the radius of curvature of the refracted ISW is estimated to be on the order of 10 km, approximately twice the incident ISW wavelength. Although the two-dimensional ISW-related convective instability is not resolved in our model, the lateral boundary may further influence the development of transverse instability (Rivera-Rosario et al., 2023), highlighting an additional avenue for future investigation.

Conflict of Interest

The authors declare no conflicts of interest relevant to this study.

Availability Statement

The raw SUNTANS output from the three-dimensional run exceeds 600 GB. Due to its size, only the cropped energetic terms within 60 km of the island are publicly available at https://doi.org/10.5281/zenodo.18470774 (Tan et al., 2026). The model code, input files needed to reproduce the simulation, and the analysis and plotting scripts are also provided in Tan et al. (2026).

Acknowledgments
This research is supported by ONR Grants N00014-24-1-2591, N00014-22-1-2040, N00014-22-1-2026, and N00014-22-1-2023. Computational resources were provided by the UC Irvine High Performance Community Computing Cluster (HPC3). The authors acknowledge Kevin Okun for his early involvement and valuable discussions. We thank Pete Diamessis and one anonymous reviewer for their insightful suggestions.

References

Aghsaee, P., Boegman, L., & Lamb, K. G. (2010). Breaking of shoaling internal solitary waves. *Journal of Fluid Mechanics*, *659*, 289–317. https://doi.org/10.1017/s002211201000248x

Alford, M. H., Peacock, T., MacKinnon, J. A., Nash, J. D., Buijsman, M. C., Centurioni, L. R., et al. (2015). The formation and fate of internal waves in the South China Sea. *Nature*, *521*(7550), 65–69. https://doi.org/10.1038/nature14399

Arthur, R. S., & Fringer, O. B. (2014). The dynamics of breaking internal solitary waves on slopes. *Journal of Fluid Mechanics*, *761*, 360–398. https://doi.org/10.1017/jfm.2014.641

Bai, X., Li, X., Lamb, K. G., & Hu, J. (2017). Internal solitary wave reflection near Dongsha Atoll, the South China Sea. *Journal of Geophysical Research: Oceans*, *122*(10), 7978–7991. https://doi.org/10.1002/2017jc012880

Becherer, J., Moum, J. N., Calantoni, J., Colosi, J. A., Barth, J. A., Lerczak, J. A., et al. (2021a). Saturation of the internal tide over the inner continental shelf. Part I: Observations. *Journal of Physical Oceanography*, *51*(8), 2553–2563. https://doi.org/10.1175/jpo-d-20-0264.1

Becherer, J., Moum, J. N., Calantoni, J., Colosi, J. A., Barth, J. A., Lerczak, J. A., et al. (2021b). Saturation of the internal tide over the inner continental shelf. Part II: Parameterization. *Journal of Physical Oceanography*, *51*(8), 2565–2582. https://doi.org/10.1175/jpo-d-21-0047.1

Bell, J. T. (1975). Topographically generated internal waves in the open ocean. *Journal of Geophysical Research*, *80*(3), 320–327. https://doi.org/10.1029/jc080i003p00320

Boegman, L., Ivey, G., & Imberger, J. (2005). The degeneration of internal waves in lakes with sloping topography. *Limnology & Oceanography*, *50*(5), 1620–1637. https://doi.org/10.4319/lo.2005.50.5.1620

Boegman, L., & Ivey, G. N. (2009). Flow separation and resuspension beneath shoaling nonlinear internal waves. *Journal of Geophysical Research*, *114*(C2). https://doi.org/10.1029/2007jc004411

Boegman, L., & Stastna, M. (2019). Sediment resuspension and transport by internal solitary waves. *Annual Review of Fluid Mechanics*, *51*(1), 129–154. https://doi.org/10.1146/annurev-fluid-122316-045049

Bolioudakis, T., Diamantopoulos, T., Diamessis, P. J., Lien, R.-C., Lamb, K. G., Rivera-Rosario, G., & Thomsen, G. N. (2026). Formation and evolution of turbulence in convectively unstable internal solitary waves of depression shoaling over gentle slopes in the South China Sea. *Journal of Physical Oceanography*, *56*(3), 533–559. https://doi.org/10.1175/jpo-d-24-0181.1

Bourgault, D., & Kelley, D. E. (2007). On the reflectance of uniform slopes for normally incident interfacial solitary waves. *Journal of Physical Oceanography*, *37*(5), 1156–1162. https://doi.org/10.1175/jpo3059.1

Bowen, A., Inman, D., & Simmons, V. (1968). Wave "set-down" and set-up. *Journal of Geophysical Research*, *73*(8), 2569–2577. https://doi.org/10.1029/jb073i008p02569

Burchard, H., & Rennau, H. (2008). Comparative quantification of physically and numerically induced mixing in ocean models. *Ocean Modelling*, *20*(3), 293–311. https://doi.org/10.1016/j.ocemod.2007.10.003

Carr, M., & Davies, P. (2010). Boundary layer flow beneath an internal solitary wave of elevation. *Physics of Fluids*, *22*(2), 026601. https://doi.org/10.1063/1.3327289

Castro-Folker, N., & Stastna, M. (2024). On the three-dimensional structure of instabilities beneath shallow-shoaling internal waves. *Journal of Fluid Mechanics*, *995*, R2. https://doi.org/10.1017/jfm.2024.703

Chang, M.-H., Cheng, Y.-H., Yang, Y. J., Jan, S., Ramp, S. R., Reeder, D. B., et al. (2021). Direct measurements reveal instabilities and turbulence within large amplitude internal solitary waves beneath the ocean. *Communications Earth and Environment*, *2*(1), 15. https://doi.org/10.1038/s43247-020-00083-6

Cheng, Y.-H., Chang, M.-H., Yang, Y. J., Jan, S., Ramp, S. R., Davis, K. A., & Reeder, D. B. (2024). Insights into internal solitary waves east of Dongsha Atoll from integrating geostationary satellite and mooring observations. *Journal of Geophysical Research: Oceans*, *129*(8), e2024JC021109. https://doi.org/10.1029/2024jc021109

Davis, K. A., Arthur, R. S., Reid, E. C., Rogers, J. S., Fringer, O. B., DeCarlo, T. M., & Cohen, A. L. (2020). Fate of internal waves on a shallow shelf. *Journal of Geophysical Research: Oceans*, *125*(5), e2019JC015377. https://doi.org/10.1029/2019jc015377

Diamantopoulos, T., Joshi, S. M., Thomsen, G. N., Rivera-Rosario, G., Diamessis, P. J., & Rowe, K. L. (2022). A high accuracy/resolution spectral element/Fourier–Galerkin method for the simulation of shoaling non-linear internal waves and turbulence in long domains with variable bathymetry. *Ocean Modelling*, *176*, 102065. https://doi.org/10.1016/j.ocemod.2022.102065

Diamessis, P. J., & Redekopp, L. G. (2006). Numerical investigation of solitary internal wave-induced global instability in shallow water benthic boundary layers. *Journal of Physical Oceanography*, *36*(5), 784–812. https://doi.org/10.1175/jpo2900.1

Dunphy, M., Subich, C., & Stastna, M. (2011). Spectral methods for internal waves: Indistinguishable density profiles and double-humped solitary waves. *Nonlinear Processes in Geophysics*, *18*(3), 351–358. https://doi.org/10.5194/npg-18-351-2011

Farmer, D. M., Alford, M. H., Lien, R.-C., Yang, Y. J., Chang, M.-H., & Li, Q. (2011). From Luzon Strait to Dongsha Plateau: Stages in the life of an internal wave. *Oceanography*, *24*(4), 64–77. https://doi.org/10.5670/oceanog.2011.95

Farmer, D. M., Li, Q., & Park, J.-H. (2009). Internal wave observations in the South China Sea: The role of rotation and non-linearity. *Atmosphere-Ocean*, *47*(4), 267–280. https://doi.org/10.3137/oc313.2009

Fringer, O., Armfield, S., & Street, R. (2005). Reducing numerical diffusion in interfacial gravity wave simulations. *International Journal for Numerical Methods in Fluids*, *49*(3), 301–329. https://doi.org/10.1002/fld.993

Fringer, O., Gerritsen, M., & Street, R. (2006). An unstructured-grid, finite-volume, nonhydrostatic, parallel coastal ocean simulator. *Ocean Modelling*, *14*(3–4), 139–173. https://doi.org/10.1016/j.ocemod.2006.03.006

Fu, K.-H., Wang, Y.-H., Laurent, L. S., Simmons, H., & Wang, D.-P. (2012). Shoaling of large-amplitude nonlinear internal waves at Dongsha Atoll in the northern South China Sea. *Continental Shelf Research*, *37*, 1–7. https://doi.org/10.1016/j.csr.2012.01.010

Garwood, J. C., Musgrave, R. C., & Lucas, A. J. (2020). Life in internal waves. *Oceanography*, *33*(3), 38–49. https://doi.org/10.5670/oceanog.2020.313

Griffies, S. M., Pacanowski, R. C., & Hallberg, R. W. (2000). Spurious diapycnal mixing associated with advection in a z-coordinate ocean model. *Monthly Weather Review*, *128*(3), 538–564. https://doi.org/10.1175/1520-0493(2000)128<0538:sdmawa>2.0.co;2

Grimshaw, R., Guo, C., Helfrich, K., & Vlasenko, V. (2014). Combined effect of rotation and topography on shoaling oceanic internal solitary waves. *Journal of Physical Oceanography*, *44*(4), 1116–1132. https://doi.org/10.1175/jpo-d-13-0194.1

Grimshaw, R. H., He, J.-M., & Ostrovsky, L. (1998). Terminal damping of a solitary wave due to radiation in rotational systems. *Studies in Applied Mathematics*, *101*(2), 197–210. https://doi.org/10.1111/1467-9590.00090

He, Y., Lamb, K. G., & Lien, R.-C. (2019). Internal solitary waves with subsurface cores. *Journal of Fluid Mechanics*, *873*, 1–17. https://doi.org/10.1017/jfm.2019.407

Helfrich, K. R. (2007). Decay and return of internal solitary waves with rotation. *Physics of fluids*, *19*(2), 026601. https://doi.org/10.1063/1.2472509

Ilıcak, M., Adcroft, A. J., Griffies, S. M., & Hallberg, R. W. (2012). Spurious dianeutral mixing and the role of momentum closure. *Ocean Modelling*, *45*, 37–58. https://doi.org/10.1016/j.ocemod.2011.10.003

Jackson, C. R., Da Silva, J. C., & Jeans, G. (2012). The generation of nonlinear internal waves. *Oceanography*, *25*(2), 108–123. https://doi.org/10.5670/oceanog.2012.46

Kang, D. (2010). Energetics and dynamics of internal tides in Monterey Bay using numerical simulations. *Doctoral dissertation*.

Kang, D., & Fringer, O. (2010). On the calculation of available potential energy in internal wave fields. *Journal of Physical Oceanography*, *40*(11), 2539–2545. https://doi.org/10.1175/2010jpo4497.1

Kang, D., & Fringer, O. (2012). Energetics of barotropic and baroclinic tides in the Monterey Bay area. *Journal of Physical Oceanography*, *42*(2), 272–290. https://doi.org/10.1175/jpo-d-11-039.1

Klingbeil, K., Mohammadi-Aragh, M., Gräwe, U., & Burchard, H. (2014). Quantification of spurious dissipation and mixing–Discrete variance decay in a Finite-Volume framework. *Ocean Modelling*, *81*, 49–64. https://doi.org/10.1016/j.ocemod.2014.06.001

la Forgia, G., Tokyay, T., Adduce, C., & Constantinescu, G. (2018). Numerical investigation of breaking internal solitary waves. *Physical Review Fluids*, *3*(10), 104801. https://doi.org/10.1103/physrevfluids.3.104801

Lamb, K. G. (2003). Shoaling solitary internal waves: On a criterion for the formation of waves with trapped cores. *Journal of Fluid Mechanics*, *478*, 81–100. https://doi.org/10.1017/s0022112002003269

Lamb, K. G. (2014). Internal wave breaking and dissipation mechanisms on the continental slope/shelf. *Annual Review of Fluid Mechanics*, *46*(1), 231–254. https://doi.org/10.1146/annurev-fluid-011212-140701

Lamb, K. G., Lien, R.-C., & Diamessis, P. J. (2019). Internal solitary waves and mixing. In J. K. Cochran, H. J. Bokuniewicz, & P. L. Yager (Eds.), *Encyclopedia of ocean sciences* (3rd ed., pp. 533–541). Academic Press. https://doi.org/10.1016/B978-0-12-409548-9.10951-0

Lamb, K. G., & Nguyen, V. T. (2009). Calculating energy flux in internal solitary waves with an application to reflectance. *Journal of Physical Oceanography*, *39*(3), 559–580. https://doi.org/10.1175/2008jpo3882.1

Lamb, K. G., & Warn-Varnas, A. (2015). Two-dimensional numerical simulations of shoaling internal solitary waves at the ASIAEX site in the South China Sea. *Nonlinear Processes in Geophysics*, *22*(3), 289–312. https://doi.org/10.5194/npg-22-289-2015

Li, Q., & Farmer, D. M. (2011). The generation and evolution of nonlinear internal waves in the deep basin of the South China Sea. *Journal of Physical Oceanography*, *41*(7), 1345–1363. https://doi.org/10.1175/2011jpo4587.1

Lien, R.-C., D'Asaro, E. A., Henyey, F., Chang, M.-H., Tang, T.-Y., & Yang, Y.-J. (2012). Trapped core formation within a shoaling nonlinear internal wave. *Journal of Physical Oceanography*, *42*(4), 511–525. https://doi.org/10.1175/2011jpo4578.1

Lien, R.-C., Henyey, F., Ma, B., & Yang, Y. J. (2014). Large-amplitude internal solitary waves observed in the northern South China Sea: Properties and energetics. *Journal of Physical Oceanography*, *44*(4), 1095–1115. https://doi.org/10.1175/jpo-d-13-088.1

Liu, Z., Zhang, W., & Helfrich, K. (2022). Vertical structure of barotropic-to-baroclinic tidal energy conversion on a continental slope. *Journal of Geophysical Research: Oceans*, *127*(9), e2022JC019130. https://doi.org/10.1029/2022jc019130

Lucas, A. J., & Pinkel, R. (2022). Observations of coherent transverse wakes in shoaling nonlinear internal waves. *Journal of Physical Oceanography*, *52*(6), 1277–1293. https://doi.org/10.1175/jpo-d-21-0059.1

Magalhaes, J. M., & Da Silva, J. C. (2018). Internal solitary waves in the Andaman Sea: New insights from SAR imagery. *Remote Sensing*, *10*(6), 861. https://doi.org/10.3390/rs10060861

McSweeney, J. M., Lerczak, J. A., Barth, J. A., Becherer, J., Colosi, J. A., MacKinnon, J. A., et al. (2020). Observations of shoaling nonlinear internal bores across the central California inner shelf. *Journal of Physical Oceanography*, *50*(1), 111–132. https://doi.org/10.1175/jpo-d-19-0125.1

Michallet, H., & Ivey, G. (1999). Experiments on mixing due to internal solitary waves breaking on uniform slopes. *Journal of Geophysical Research*, *104*(C6), 13467–13477. https://doi.org/10.1029/1999jc900037

Miles, J. W., & Huppert, H. E. (1969). Lee waves in a stratified flow. Part 4. Perturbation approximations. *Journal of Fluid Mechanics*, *35*(3), 497–525. https://doi.org/10.1017/s0022112069001248

Ramp, S., Yang, Y., & Bahr, F. (2010). Characterizing the nonlinear internal wave climate in the northeastern South China Sea. *Nonlinear Processes in Geophysics*, *17*(5), 481–498. https://doi.org/10.5194/npg-17-481-2010

Ramp, S., Yang, Y.-J., Jan, S., Chang, M.-H., Davis, K., Sinnett, G., et al. (2022). Solitary waves impinging on an isolated tropical reef: Arrival patterns and wave transformation under shoaling. *Journal of Geophysical Research: Oceans*, *127*(3), e2021JC017781. https://doi.org/10.1029/2021jc017781

Ramp, S. R., Tang, T. Y., Duda, T. F., Lynch, J. F., Liu, A. K., Chiu, C.-S., et al. (2004). Internal solitons in the northeastern South China Sea. Part I: Sources and deep water propagation. *IEEE Journal of Oceanic Engineering*, *29*(4), 1157–1181. https://doi.org/10.1109/joe.2004.840839

Reid, E. C., DeCarlo, T. M., Cohen, A. L., Wong, G. T., Lentz, S. J., Safaie, A., et al. (2019). Internal waves influence the thermal and nutrient environment on a shallow coral reef. *Limnology & Oceanography*, *64*(5), 1949–1965. https://doi.org/10.1002/lno.11162

Rivera-Rosario, G., Diamessis, P. J., Lien, R.-C., Lamb, K. G., & Thomsen, G. N. (2023). Three-dimensional perspective on a convective instability and transition to turbulence in an internal solitary wave of depression shoaling over gentle slopes. *Environmental Fluid Mechanics*, *23*(5), 1015–1035. https://doi.org/10.1007/s10652-022-09844-7

Rogers, J. S., Mayer, F. T., Davis, K. A., & Fringer, O. B. (2022). On internal tides driving residual currents and upwelling on an island. *Journal of Geophysical Research: Oceans*, *127*(7), e2021JC018261. https://doi.org/10.1029/2021jc018261

Rogers, J. S., Rayson, M. D., Ko, D. S., Winters, K. B., & Fringer, O. B. (2019). A framework for seamless one-way nesting of internal wave-resolving ocean models. *Ocean Modelling*, *143*, 101462. https://doi.org/10.1016/j.ocemod.2019.101462

Rogers, J. S., Tan, S., Davis, K. A., Pawlak, G., & Fringer, O. B. (2025). Climate-driven stratification intensifies internal wave cooling on a shallow island reef. *Geophysical Research Letters*, *52*(14), e2025GL115458. https://doi.org/10.1029/2025gl115458

Sakai, T., Diamessis, P. J., & Jacobs, G. B. (2020). Self-sustained instability, transition, and turbulence induced by a long separation bubble in the footprint of an internal solitary wave. I. Flow topology. *Physical Review Fluids*, *5*(10), 103801. https://doi.org/10.1103/physrevfluids.5.103801

Shepherd, T. G. (1993). A unified theory of available potential energy. *Atmosphere-Ocean*, *31*(1), 1–26. https://doi.org/10.1080/07055900.1993.9649460

Shroyer, E. L., Moum, J. N., & Nash, J. D. (2011). Nonlinear internal waves over New Jersey's continental shelf. *Journal of Geophysical Research*, *116*(C3), C03022. https://doi.org/10.1029/2010jc006332

Sinnett, G., Ramp, S. R., Yang, Y. J., Chang, M.-H., Jan, S., & Davis, K. A. (2022). Large-amplitude internal wave transformation into shallow water. *Journal of Physical Oceanography*, *52*(10), 2539–2554. https://doi.org/10.1175/jpo-d-21-0273.1

Stastna, M., & Lamb, K. G. (2002). Large fully nonlinear internal solitary waves: The effect of background current. *Physics of fluids*, *14*(9), 2987–2999. https://doi.org/10.1063/1.1496510

Stastna, M., & Legare, S. (2024). Simulations of shoaling large-amplitude internal waves: Perspectives and outlook. *Flow*, *4*, Ec11. https://doi.org/10.1017/flo.2024.9

St. Laurent, L. (2008). Turbulent dissipation on the margins of the South China Sea. *Geophysical Research Letters*, *35*(23), L23615. https://doi.org/10.1029/2008GL035520

Sutherland, B., Barrett, K., & Ivey, G. (2013). Shoaling internal solitary waves. *Journal of Geophysical Research: Oceans*, *118*(9), 4111–4124. https://doi.org/10.1002/jgrc.20291

Tan, S., Rogers, J., Fringer, O., Pawlak, G., Chang, Y., & Davis, K. (2026). Dataset supporting to the paper "Energetics of internal solitary waves interacting with a conical Island. *Zenodo*. https://doi.org/10.5281/zenodo.18470774

Trowbridge, J. H., Helfrich, K. R., Reeder, D. B., Medley, G., Chang, M.-H., Jan, S., et al. (2025). Observations of the bottom boundary layer beneath the world's largest internal solitary waves. *Journal of Geophysical Research: Oceans*, *130*(3), e2024JC022028. https://doi.org/10.1029/2024jc022028

Venayagamoorthy, S., & Fringer, O. (2005). Nonhydrostatic and nonlinear contributions to the energy flux budget in nonlinear internal waves. *Geophysical Research Letters*, *32*(15), L15603. https://doi.org/10.1029/2005gl023432

Venayagamoorthy, S. K., & Fringer, O. (2006). Numerical simulations of the interaction of internal waves with a shelf break. *Physics of Fluids*, *18*(7), 076603. https://doi.org/10.1063/1.2221863

Venayagamoorthy, S. K., & Fringer, O. B. (2007). On the formation and propagation of nonlinear internal boluses across a shelf break. *Journal of Fluid Mechanics*, *577*, 137–159. https://doi.org/10.1017/s0022112007004624

Vitousek, S., & Fringer, O. B. (2011). Physical vs. numerical dispersion in nonhydrostatic ocean modeling. *Ocean Modelling*, *40*(1), 72–86. https://doi.org/10.1016/j.ocemod.2011.07.002

Vlasenko, V., & Stashchuk, N. (2007). Three-dimensional shoaling of large-amplitude internal waves. *Journal of Geophysical Research*, *112*(C11), C11018. https://doi.org/10.1029/2007jc004107

Voet, G., Alford, M. H., Cusack, J. M., Pratt, L. J., Girton, J. B., Carter, G. S., et al. (2023). Energy and momentum of a density-driven overflow in the Samoan passage. *Journal of Physical Oceanography*, *53*(6), 1429–1452. https://doi.org/10.1175/jpo-d-22-0220.1

Wang, Y., & Legg, S. (2023). Enhanced dissipation of internal tides in a mesoscale baroclinic eddy. *Journal of Physical Oceanography*, *53*(10), 2293–2316. https://doi.org/10.1175/jpo-d-23-0045.1

Xu, C., & Stastna, M. (2020). Instability and cross-boundary-layer transport by shoaling internal waves over realistic slopes. *Journal of Fluid Mechanics*, *895*, R6. https://doi.org/10.1017/jfm.2020.389

Zhang, Z., Fringer, O., & Ramp, S. (2011). Three-dimensional, nonhydrostatic numerical simulation of nonlinear internal wave generation and propagation in the South China Sea. *Journal of Geophysical Research*, *116*(C5), C05022. https://doi.org/10.1029/2010jc006424

Zilberman, N., Becker, J., Merrifield, M., & Carter, G. (2009). Model estimates of M2 internal tide generation over Mid-Atlantic Ridge topography. *Journal of Physical Oceanography*, *39*(10), 2635–2651. https://doi.org/10.1175/2008jpo4136.1